

Geometry Sensitivity Study of a Recently-Maneuvered Satellite

Dylan R. Penn

Virginia Polytechnic Institute and State University

Cameron Harris, Dr. Kevin Schroeder, Dr. Jonathan Black

Virginia Polytechnic Institute and State University

ABSTRACT

Maintaining knowledge of the current and future locations of resident space objects (RSOs) is a critical focus of space traffic management (STM). This paper seeks to identify regions of an orbital pass over a ground-based sensor that are conducive to the detection of orbital trajectory changes. The ideal observation would be that made at the point when apparent angular separation from the expected trajectory is maximized. A ground site overflight model was built to characterize the apparent separation between an expected and perturbed trajectory of the satellite. The geometry of an overflight was parameterized in terms of rise point and relative heading. An algorithm was developed to define initial conditions of the satellites which span all possible pass geometries. Given a positive-velocity maneuver, trajectories which progress nearly-directly overhead of a ground site experience a “catch-up” effect, where the lower trajectory catches up and overtakes the higher orbit. The catch-up effect can be characterized, given a selected maximum angular separation, by a convex region in azimuth-elevation space. Angular separation is maximized when viewed during the middle portion of the pass, whereas range separation is maximized at the end of a pass. Changes in altitude or maneuver magnitude do not meaningfully impact the trends of angular or range separation in time or space.

1. INTRODUCTION

Maintaining knowledge of the current and future locations of resident space objects (RSOs) is a critical focus of space traffic management. Accurate state knowledge of RSOs is important for the preservation and continued use of space. The full catalog of RSOs is largely maintained by ground-based radar and optical sensors, which selectively observe RSOs as they pass overhead. The RSO catalog is rapidly expanding, with an increasing number of actors entering in the space domain. The European Space Agency (ESA) currently estimates the number of identified RSOs to exceed 26,000 – a growth of nearly 5,000 objects in three years [1]. In 2018, the Department of Commerce (DOC) was charged with the space traffic management (STM) mission, although the transfer from the United States Space Force (USSF) has not yet completed [2–5].

The growing catalog of space objects brings with it an equal concern for orbital safety, especially given the increase in active spacecraft. Prior notification of maneuver activity to the DOC or USSF is requested but ultimately voluntary [6]. Therefore, it is up to the STM authority to detect when a maneuver occurs and update the catalog accordingly. Failure to detect non-cooperative maneuvers in a timely manner can result in difficulty correlating tracks or even duplicated RSOs [7, 8] In general, any maneuver (or lack thereof) that occurs outside of the STM authority’s plan can be considered non-cooperative. Furthermore, it cannot be guaranteed that a satellite operator will always accurately know the orbital state of their own spacecraft.

Generally, active spacecraft in all orbital regimes perform station-keeping maneuvers to maintain their mission. As technology advances, fuel budgets will become less restrictive, and orbital maneuvers will become more frequent. As maneuvers become more commonplace, the tasking and scheduling of space surveillance sensors must be planned intelligently.

The goal of this research is to examine the geometry of an RSO flyover of a ground-based sensor as it pertains to the detectability of orbital state changes. Assuming perfect measurements, any difference in observations from the expected trajectory indicates that a non-cooperative maneuver has occurred, and that the orbital state in the RSO catalog must be updated. In particular, this research investigates the evolution of the physical geometry of a sensor observation of an RSO during a pass. This paper seeks to identify regions of an orbital pass over a ground-based sensor that are conducive to the detection of orbital trajectory changes. The results can inform future STM efforts for sensor tasking and management, as it pertains to maneuver detectability.

The paper is organized into five sections. The first section overviews the contemporary STM practices and inherent challenge of tracking maneuvering spacecraft. The second section gives a brief background on space surveillance sensor observations and their relevance to sensor tasking. The third section provides a methodological breakdown of orbit pass geometry and modelling of maneuvered satellite passes in a simulated environment. The fourth section presents and analyzes the results from orbital pass simulations. The fifth section summarizes pertinent findings and identifies important takeaways.

2. BACKGROUND

The position of a ground-based sensor is denoted as \vec{r}_{site} . The position of a spacecraft is denoted as \vec{r} . Unless indicated otherwise, all vectors in this paper are written in the Earth-Centered Inertial (ECI) frame. Azimuth, β , and elevation, el , are angles which are used to describe the line-of-sight vector of a spacecraft relative to a ground-based sensor in the Topocentric-Horizon Coordinate System (SEZ) frame. Azimuth is measured from North, increasing towards East; elevation is measured from the horizon, increasing towards zenith. The field of regard (FOR) of a ground-based sensor, ignoring location-dependent geophysical constraints, covers 360° azimuth and 90° of elevation; i.e., :

$$0^\circ \leq \beta < 360^\circ \quad (1)$$

$$0^\circ \leq el < 90^\circ \quad (2)$$

Range, ρ , is not directly available to an optical sensor, but it is available to a radar or laser ranging sensor.

The orbital state of a satellite is a six-dimensional state vector. It is frequently treated as the combination of its three-dimensional ECI position and velocity: $[\vec{r}, \vec{v}]$. The measured position of a satellite, \vec{r}^{SEZ} , is β , el , and ρ mapped to the SEZ frame. A full description of the transformation between \vec{r} , azimuth and elevation (β and el), and \vec{r}^{SEZ} is shown by Vallado in [9]. The expected azimuth and elevation from a propagated orbital state can be used to determine windows of time when the spacecraft will be in line-of-sight of the sensor. Line-of-sight windows are needed to develop a tasking schedule for a sensor network.

Because catalog maintenance of RSO is a resource-constrained problem, sensors should be tasked judiciously. When there are overlapping visibility windows, spacecrafts are tasked based on priority. Historically, spacecraft priorities were sorted into classifications based on the spacecrafts' apogee and perigee, known as Gabbard classes. Presently, spacecraft priorities are organized into categories based on several metrics, rather than just the orbit regime. Contemporary tasking operations allocate sensors based on an optimization of the expected number of tracks and spacecraft priority. A complete discussion of the historic and contemporary practices of space surveillance sensor tasking can be found in [10]. Some proposed future methods of tasking sensors include covariance information to determine spacecraft tasking priority [11, 12]. Both contemporary and proposed future methods for sensor allocation place constraints on the minimum allowable elevation angle, but there is otherwise no direct consideration of the pass geometry.

Depending on the range of the spacecraft from the sensor, geometric separation from an expected trajectory transforms non-linearly into angular separation in azimuth-elevation space. Given the complex geometric interaction of mapping \vec{r} to β and el , it stands to reason that not all observation geometries are equally useful for identifying a difference from the expected trajectory. Ostensibly, the ideal observation (for an optical sensor at least, and a radar sensor potentially) would be that made at the point when apparent angular separation from the expected trajectory is maximized. With angular separation maximized, it could more easily be determined whether or not the spacecraft had appreciably deviated from its expected trajectory.

In the maneuver scenario, the azimuth/elevation of a spacecraft influences the apparent angular separation θ of the spacecraft from its nominal trajectory. It is easier to identify a deviation from an expected trajectory for larger values of θ . For a given orbit, the range between the ground site and satellite ρ varies depending on where the satellite is in the hemisphere centered on the ground site (e.g. small ρ for a satellite directly overhead vice large ρ for a satellite far off on the horizon). To identify a maneuver, it is not simply a function of the magnitude of maneuver, but the geometry of the nominal trajectory relative to the ground site (i.e. distance and orientation).

This point is apparent from the arc length formula:

$$s = \rho\theta \quad (3)$$

where s is the arc length, ρ is the distance from the center of the circle described by the arc, and θ is the angular separation between the endpoints of the arc. In this instance, the distance ρ is the range from a sensor to a spacecraft, $|\vec{r} - \vec{r}_{site}|$. The length of the arc s is a linear projection of the relative separation between the expected and observed trajectories at an instance in time. The apparent angular separation θ is maximized when the ratio $\frac{s}{\rho}$ is maximized. At first glance, it would appear that an observation would be most effective at revealing angular separation when $|\vec{r} - \vec{r}_{site}|$ is minimized – however, the projected relative separation, s , of two trajectories can change significantly during a flyover, depending on the geometry of the trajectories relative to the ground sensor.

In summary, it is apparent that the relative geometry of a sensor and a spacecraft influences the sensor's ability to detect changes in the spacecraft's orbital state. As the azimuth and elevation of the spacecraft evolve over the duration of a pass, there may be geometries where an observation of the spacecraft would be more conducive to detecting changes, should a maneuver or other perturbation have occurred. However, the relative pass geometry is not directly considered in contemporary space surveillance sensor tasking schemes.

3. METHODOLOGY

A model was built to simulate a satellite overflight of a single ground site to characterize the apparent separation between an expected and perturbed trajectory. To cover the span of possible pass geometries, the geometry of an overflight was parameterized in terms of rise point and relative heading (terms which are elaborated on subsequently). An algorithm was developed to define initial conditions of the satellites to span pass geometries. This section details the parameterization of the overflight geometry and the derivation of satellite initial conditions, defines the metrics used in the study, and describes the parameters used in the simulations.

3.1 Reducing Design Space

The geometry of a single orbital pass is first parameterized to narrow the span of initial conditions which would represent the full diversity of geometry of passes relative to a ground site. The geometry of a single pass can be defined by a chord connecting two points on the circular horizon and the distance from the center of the circle (the ground station) to the midpoint of the chord. For the orbital pass scenario, it is desirable to reduce the range of chords to examine; this reduction is completed via two mechanisms.

First, for a ground sensor with no azimuth restrictions, holding orbit geometry constant, and assuming a non-rotating Earth, a South-to-North pass is identical to a North-to-South, East-to-West, and indeed all other pass geometries in terms of elevation evolution. This property reduced the design space to only those passes which start at a single point on the horizon. The non-rotating Earth assumption is valid if viewing geometry (azimuth/elevation) from the ground station is not severely impacted by Earth's rotation. Given the large distances from the ground station to orbit, small distances between two recently-diverged orbital trajectories, and short time window of interest (for Low Earth Orbit (LEO) satellites), the non-rotating Earth assumption seems reasonable. This assumption is validated in Section 4.1.

Second, the chord congruency theorem is applied. Chords that are equidistant from the center of a circle are equal in length. This allows only half of the possible chords of a circle to be considered. By combining both the single rise point property and the chord congruency theorem, all pass geometries can be represented by a range of chords which have a single common rise point and a range of set points starting 180° opposite the rise point (this first chord being the diameter of the circle) spanning half of the perimeter of the circle. This reduction in pass geometries is illustrated in Figure 1.

The range of ground tracks (chords) is represented by initializing all orbits at a point on the horizon relative to the ground sensor, with relative headings $\psi \in [0, \pi/4]$ radians, where $\psi = 0$ represents a ground track going directly over the sensor (the diameter of the circle defined by the horizon), and $\psi = \pi/4$ is a ground track which is a point on the horizon (a chord of infinitesimal length). The chosen rise point is arbitrary; due South of the ground sensor was chosen for convenience in aligning $\psi = 0$ with North. Relative heading is not constant throughout a pass; this paper is only concerned with *initial* relative heading. The term “relative heading” is used here to distinguish that the parameter is different from “true heading”, which is typically based on cardinal direction. True heading is not used in this paper. Going forward, the term “initial heading” is used for brevity in place of “initial relative heading.”

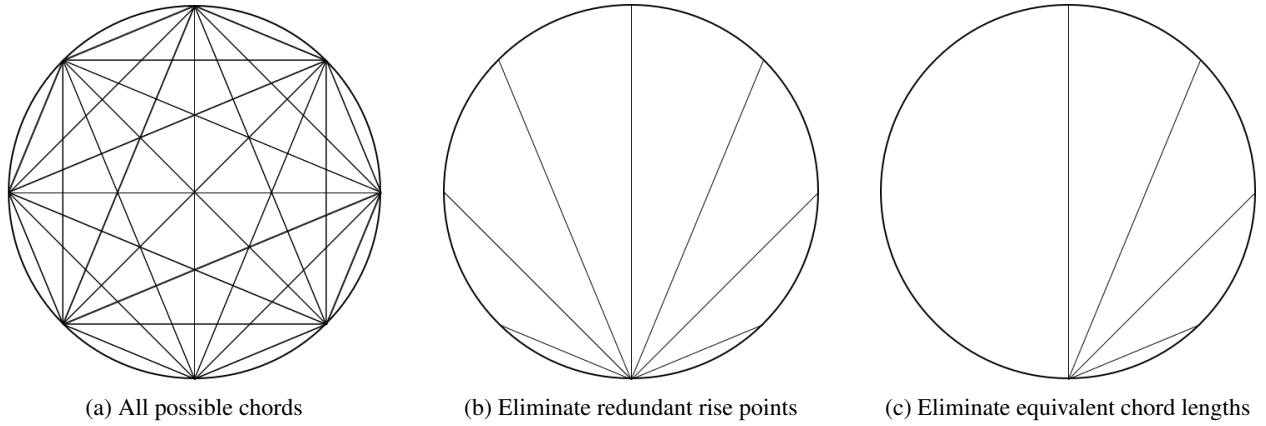


Fig. 1: The range of possible ground tracks can be reduced to a single rise point and a range of relative headings ψ .

3.2 Initial Conditions

First the initial satellite position relative to the ground site is defined for all simulations. For all simulation runs, a ground sensor geodetic latitude was specified, giving the position vector of the site \vec{r}_{site} . For reasons that are detailed later, the ground site altitude was restricted to the surface of a spherical Earth. A circular orbit size was defined by setting an orbit altitude h and corresponding position and velocity magnitudes r and v , respectively; only circular orbits were considered in this analysis.

First, we must determine the magnitude of the initial slant range ρ_0 . From r , the magnitude of the position vector of the ground site r_{site} , and assuming the initial slant range vector $\vec{\rho}_0$ is perpendicular to \vec{r}_{site} , we can determine the initial position vector magnitude of the satellite r_0 using trigonometric relationships. The trigonometric relationship between \vec{r}_0 , \vec{r}_{site} , and $\vec{\rho}_0$ is illustrated in Figure 2. Pythagorean Theorem gives the magnitude of the initial slant range vector as

$$\rho_0 = \sqrt{r_0^2 - r_{site}^2}. \quad (4)$$

The perpendicular assumption between \vec{r}_{site} and $\vec{\rho}_0$ requires that the ground station be located on the surface of a spherical Earth; if the ground site altitude were higher than the Earth ellipsoid, the rise point would be lower than the local horizon, meaning that \vec{r}_{site} and $\vec{\rho}_0$ would not be perpendicular. For this study, the perpendicularity assumption is a minor one because we are mainly concerned with the evolution of the slant range vector $\vec{\rho}$, which is not greatly impacted by the small angle differences that arise from nonzero site altitude.

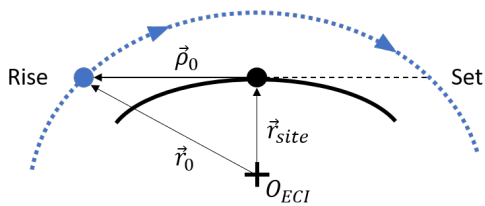


Fig. 2: Initial position \vec{r}_0 was calculated by specifying r , the site location \vec{r}_{site} , and constraining initial slant range $\vec{\rho}_0$ to be due South of the ground site.

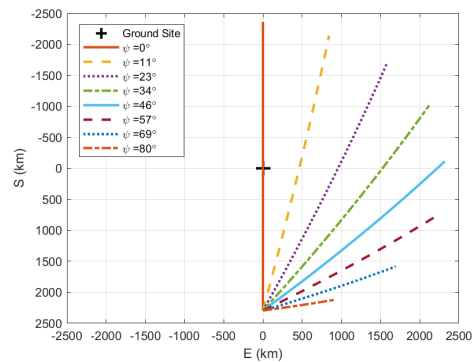


Fig. 3: Notional ground tracks of nominal orbits, assuming a non-rotating Earth. The ground site is located at $[0,0]$.

We define the initial slant range vector in the SEZ frame as

$$\vec{\rho}_0^{SEZ} = \left[\sqrt{r_0^2 - r_{site}^2}, 0, 0 \right]^T. \quad (5)$$

Note that the scalar r_{site} is constant regardless of reference frame and the vector \vec{r}_{site} is constant in the SEZ and Earth-Centered-Earth-Fixed (ECEF) frames. The initial slant range vector $\vec{\rho}_0^{SEZ}$ can be transformed from SEZ to ECI using the method described by Vallado in [9]. With $\vec{\rho}_0$ and \vec{r}_{site} known, we also have \vec{r}_0 from the standard coordinate transformation.

With the initial position determined, which is the same for all orbits, initial velocity \vec{v}_0 is calculated next, which is the primary parameter varied across simulation runs. The initial velocity of the orbit which passes directly over the ground site ($\psi = 0$) is called the *overhead orbit*. Because only circular orbits are considered, \vec{v}_0 is perpendicular to \vec{r}_0 (and more generally $\vec{v} \perp \vec{r}$ for all time). $\vec{v}_{0,overhead}$ is calculated by multiplying v by the cross product of $\hat{r}_0 \times \hat{r}_{site}$ and \hat{r}_0 , or more compactly

$$\vec{v}_{0,overhead} = v(\hat{r}_0 \times \hat{r}_{site}) \times \hat{r}_0, \quad (6)$$

where $\hat{\cdot}$ is the unitized vector.

Next, the initial velocities are calculated for orbits which do not pass directly overhead of the sensor, i.e. orbits where $\psi \neq 0$. For each perturbed orbit, $\vec{v}_{0,overhead}$ is rotated about the N-vector in the satellite-relative normal-tangential-cross-plane (NTW) frame (note that the N-vector in the NTW frame points toward the center of the Earth because the orbits in this study are circular, although this is not the case generally) [9]. This yields a set of \vec{v}_0 vectors that correspond to ground track resembling the half-fan shape in Figure 1c. Note that all initial velocities have the same magnitude.

Summarizing, we now have a set of circular orbits with a common initial position located due South on the local horizon of the ground site, and a set of initial velocities which, when propagated, generate ground tracks that create a half-fan pattern, which is illustrated in Figure 3. In classical orbital elements space, this set of orbits all have identical semi-major axis (SMA) and eccentricity ($e = 0$), but different inclination and right ascension of ascending node. Taken together, we call this set of orbits the *nominal orbits*. Next, we introduce *perturbed orbits*.

3.3 Perturbed Orbits

The set of nominal orbits are the “expected” orbits in the simulation. To generate “unexpected” orbits, the nominal set of initial conditions is perturbed. An impulsive ΔV of $10m/s$ in the positive-velocity direction is applied at the rise point of each nominal trajectory. The initial velocity of each perturbed orbit is

$$\vec{v}_{0,perturbed}^{NTW} = \vec{v}_{0,nominal}^{NTW} + [0, \Delta V, 0]^T. \quad (7)$$

Summarizing, each of the nominal orbit is paired with a perturbed orbit, where each perturbed orbit has the same initial position $\vec{r}_{0,nominal} = \vec{r}_{0,perturbed}$ as its partner nominal orbit, but a different initial velocity $\vec{v}_{0,nominal} \neq \vec{v}_{0,perturbed}$. The algorithm to generate initial conditions for an orbital pass given a ground site and circular orbit altitude is given in appendix A. An ensemble of nominal and perturbed orbits is illustrated in Figure 4.

3.4 Metrics

The two metrics used to characterize the change in geometry of the nominal and perturbed trajectories are angular separation θ and range separation $\Delta\rho$, illustrated in Figure 5. Angular separation is defined as the angle between the unitized slant range vectors of the nominal and perturbed trajectories at time t , $\hat{\rho}(t)_{nominal}$ and $\hat{\rho}(t)_{perturbed}$, respectively. Range separation is defined as the difference in slant range magnitude between the ground site and the two satellites at time t , or

$$\Delta\rho = \rho_{nominal} - \rho_{perturbed}. \quad (8)$$

Note that the sign of $\Delta\rho$ indicates which satellite is closer to the ground site (positive for the nominal trajectory being closer). Because the scenario begins with both satellites co-located, the initial values of both θ and $\Delta\rho$ are always 0.

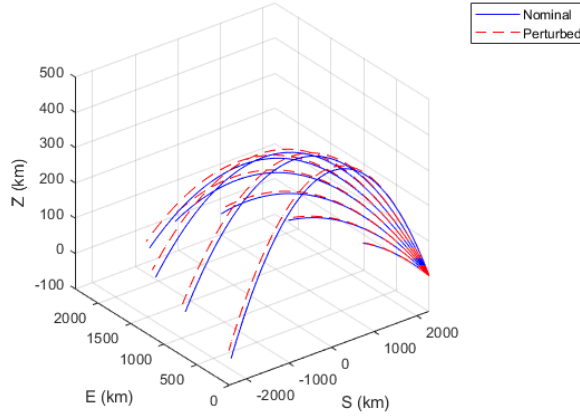


Fig. 4: An illustration of the ensemble of nominal (blue solid lines) and perturbed (red dashed lines) orbits in the SEZ frame ($[0,0,0]$ is the ground site).

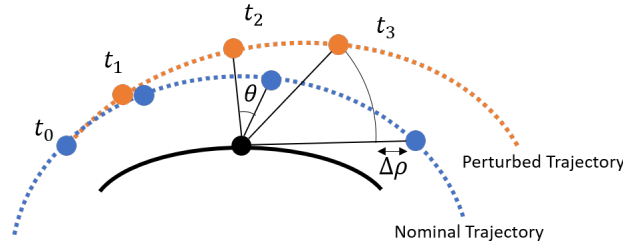


Fig. 5: Illustration of angular separation θ and range separation $\Delta\rho$.

3.5 Simulation

Each simulation propagated a nominal-perturbed orbit pair from rise to set over a ground site. To validate the non-rotating Earth assumption (see Section 3.1), each simulation was run with both a rotating and non-rotating Earth, and with a ground site latitude of $\phi = \{0, 70^\circ\}$. The initial position for all simulations was $\vec{p}_0^{SEZ} = [\rho_0, 0, 0]^T$. Note that the initial position in the ECI frame \vec{r}_0 differed depending on ground site latitude. Initial headings were linearly spaced from $\psi = [0, 80^\circ]$; initial headings near 90° resulted in too short of a pass to provide meaningful data. Line plots in this paper use eight initial headings; contour plots were generated using thirty initial headings, although less are shown on said plots for readability. Orbit magnitudes of $r = \{400, 600, 800, 1000\}km$ were simulated. Unless otherwise noted, a maneuver magnitude of $\Delta V = 10m/s$ was used. Dynamics were propagated at 10 second time steps and assuming 2-body motion.

4. RESULTS AND ANALYSIS

This section presents and analyzes the results, in terms of angular separation θ and range separation $\Delta\rho$, of the simulations outlined in Section 3.5. First, the assumptions (non-rotating Earth, ground site latitude) used to define the initial conditions are addressed. Second, θ and $\Delta\rho$ are examined for a baseline orbit altitude ($h = 400km$). Then, the preceding trends are compared across different altitudes. Last, impacts of ΔV are examined.

4.1 Effects of Earth Rotation and Ground Site Latitude

First, the assumption in Section 3.1 that the effects of Earth's rotation and ground site latitude do not have a significant effect on satellite azimuth/elevation evolution over the pass must be validated. The nominal orbits were simulated at $h = 400km$ altitude with Earth rotation both on and off, and with ground sites located at 0° and 70° latitude. In both cases, differences in state evolution between the control (static Earth, equatorial ground site) and experimental cases

(rotating Earth, high-latitude ground site) were very small; trajectory plots are not visibly distinguishable, and are not shown. Therefore, the initial conditions chosen for this study (a single rise point and a half-fan of initial headings) are valid to observe trends over a single orbital pass. Going forward, all analysis is presented with a rotating Earth and equatorial ground site.

4.2 Baseline Case

Angular Separation Trends Figure 6 shows the baseline case ($h = 400\text{km}$, $\Delta V = 10\text{m/s}$) of angular separation between nominal and perturbed orbits, as observed from the equatorial ground site, plotted against the South component of the sub-satellite point. This reference frame (along the South direction) is useful for comparison to different orbit altitudes (Section 4.3). Three observations can be made of this data.

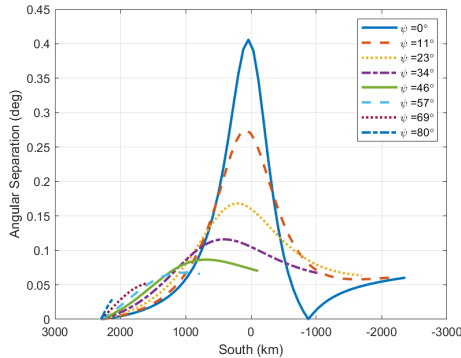


Fig. 6: Angular separation between the nominal and perturbed trajectories as observed from the ground site ($h = 400\text{km}$, $\Delta V = 10\text{m/s}$).

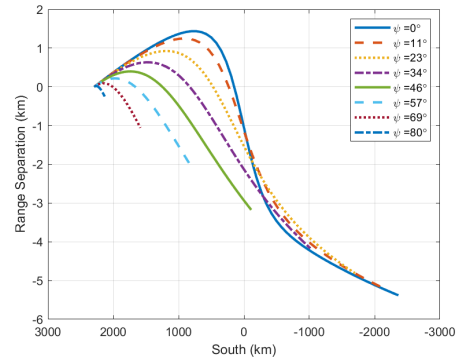


Fig. 7: Range separation between the nominal and perturbed trajectories as observed from the ground site ($h = 400\text{km}$, $\Delta V = 10\text{m/s}$).

Initial heading is negatively correlated with pass duration; direct-overhead passes last longer than passes far off on the horizon. This is an effect of the nominal orbit trajectory, unrelated to the perturbed orbit.

Peak angular separation is negatively correlated with initial heading; the peak angular separation of each trajectory pair decreases in magnitude as passes move from direct-overhead to barely in-view. This effect is caused by the relation of the large slant ranges to small satellite separation distances. For larger slant ranges, such as those caused by low initial headings, the relatively small distance between the two satellites (nominal and perturbed) results in a small angular separation. For smaller slant ranges, i.e. lower initial headings, the opposite is true. Summarizing, due to the high ratio of slant range to relative distance, angular separation increases and peaks as the nominal and perturbed trajectories approach their respective zenith points.

Of particular note in Figure 6 is the sharp decline and recovery of angular separation for the direct overhead pass ($\psi = 0^\circ$) at around -750km . This phenomenon, which dubbed here as the “catch-up” effect, is caused by a combination of the pass geometry and the particular maneuver chosen for this simulation. Soon after the maneuver, relative separation increases between the two trajectories, corresponding to an increase in angular separation, much like the $\psi \neq 0^\circ$ trajectories. As in those other trajectories, angular separation peaks at the minimum slant range (directly overhead). However, in the $\psi = 0^\circ$ case, the ground site lies on the orbital planes of both the nominal and perturbed trajectories (recall that the maneuver is in the positive-velocity direction, meaning that the orbits are coplanar). This alignment makes both trajectories appear to the ground site to move on a line. The perturbed trajectory, due to its larger SMA relative to the nominal trajectory, moves slower along this line than the nominal trajectory. The catch-up point is the point at which the lower orbit (nominal orbit) overtakes the perturbed trajectory. The catch-up effect is not observed in Figure 6 for the other trajectory pairs because in those cases the ground station does not lie on the orbital planes. If a maneuver direction that caused the two orbits to not be coplanar, the catch-up effect would not be observed for even the $\psi = 0$ case. Next, the sensitivity of the catch-up effect with respect to initial heading ψ is examined.

Although catch-up events occur only for direct-overhead passes, trajectories near $\psi \approx 0$ still experience some degree of the catch-up effect. By setting an upper bound on θ , a catch-up region in azimuth-elevation space can be described. Figure 8 shows θ contours on azimuth-elevation axes, with initial headings overlaid as dashed lines. The $\theta < 0.05^\circ$ bound on the left side of the figure is the catch-up region, where the catch-up effect is convexly bounded (convexity

is true for slightly larger values of θ but, 0.05° was chosen for convenience). Using this definition of a catch-up region, trajectories with initial heading $\psi \lesssim 8.3^\circ$ experience the catch-up effect. The catch-up region is bounded by $5.4^\circ < el < 29.9^\circ$ and $0^\circ < \beta < 20.4^\circ$. This region, although not pictured, is symmetric about $\beta = 0$ because trajectories with initial headings $\psi = \pm x$ have identical θ histories (neglecting Earth rotation effects). This symmetry doubles the azimuth bounds of the catch-up region in Figure 8. These bounds describe a 40.7° -azimuth by 24.4° -elevation region, centered at $el = 17.7^\circ$ and an arbitrary azimuth, within which the perturbed trajectory is within 0.05° of the nominal trajectory when viewed from the ground site. Depending on the needs of the analysis, the threshold for θ can be adjusted to find a corresponding region with tighter/looser restrictions. Describing the catch-up region as azimuth-elevation bounds is a compact and easy-to-understand representation, but it should be noted that the actual shape of the catch-up region in azimuth-elevation space is more complex; for small values of θ it is a rough oval, while for larger values of θ the shape becomes more like that of a bent oval.

The trends in angular separation discussed above are useful for the STM mission given an angles-only sensor in three respects. First, assuming the objective of a sensor is to detect a maneuver of the type studied here, the location of the catch-up region on the descending portion of the pass can inform the sensor tasking engine to deprioritize that azimuth-elevation region of the sky because a maneuver would be more difficult to detect. Second, the characterization of azimuth-elevation ranges which have high angular separations can inform the tasking engine as to which areas of the sky to search to have the best probability (when considering only the dynamics) of detecting a maneuver. Roughly speaking, the middle portion of a given pass has the highest angular separation, meaning the best opportunity for maneuver detection. Last, in a scenario in which the objective is to detect closely-spaced objects (CSOs), a tasking engine could use knowledge of the the catch-up region to prioritize other areas of the sky to search, where angular separation is greater.

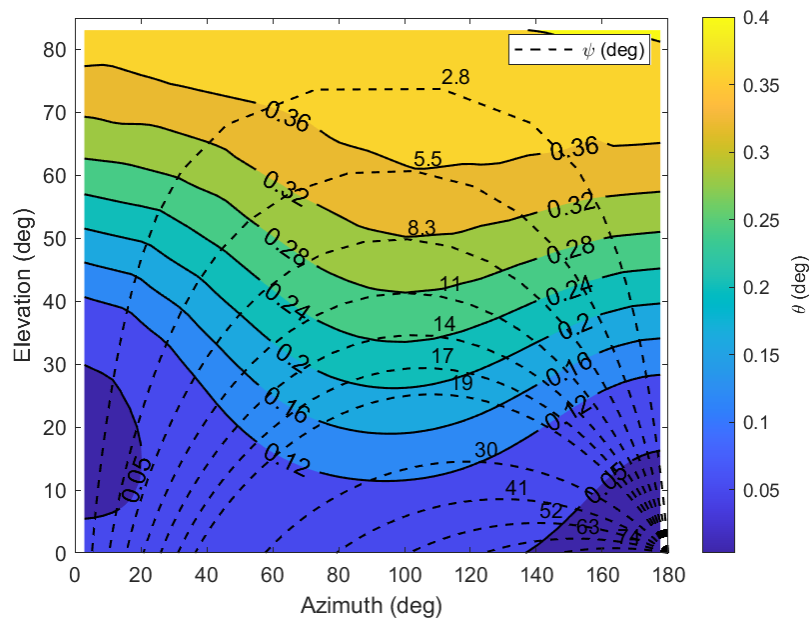


Fig. 8: Lines of initial heading ψ are overlaid on angular separation contours. All trajectories start at $\beta = 180^\circ, el = 0^\circ$. Elevation and azimuth correspond to nominal trajectories ($h = 400\text{km}, \Delta V = 10\text{m/s}$).

Range Separation Trends Figure 7 is the range separation equivalent of Figure 6. Recall that range separation is defined as $\Delta\rho = \rho_{nominal} - \rho_{perturbed}$, where ρ is the slant range from the ground site to the satellite. Positive values of $\Delta\rho$ indicate that the perturbed trajectory is closer to the ground site than the nominal trajectory at that time ($\rho_{perturbed} < \rho_{nominal}$).

The largest absolute range separations ($\Delta\rho \lesssim -5\text{km}$ in the near direct-overhead passes) occur at the set points. As the trajectories diverge, the magnitude of range separation increases until the perturbed orbit reaches apogee, after which

the trajectories converge to a shared perigee. Because the time period of interest is much less than half-an orbit, we observe only the divergence of trajectories in this plot.

All trajectory pairs (initial headings) start with the perturbed satellite being closer to the ground site than the nominal satellite (increasing $\Delta\rho$) before hitting a maximum, after which range separation decreases monotonically through the remainder of the pass (decreasing $\Delta\rho$). This increasing-decreasing trend is most visible in Figure 7 for low values of ψ , but the trend exists for all trajectory pairs. There is a sort of “catch-up” effect in range separation, although with different features and caused by a different mechanism than that of angular separation. For one, the range separation catch-up effect is present for all initial headings. Secondly, the range separation catch-up effect does not have the rise-fall-rise pattern of the angular separation effect; range separation trends simply as rise-fall. This difference in sign pattern is due to the representation of $\Delta\rho$; it is the difference of two position vectors taking on all values $\Delta\rho \in (-\infty, \infty)$, whereas θ is constrained to $\theta \geq 0$. The absolute value could be taken of $\Delta\rho$ to emulate the rise-fall-rise pattern of range separation, but one would lose insight into which trajectory is closer to the ground site (without needing another metric). Also note that the zero-separation crossing points occurs earlier in the pass for range separation compared to angular separation; all catch-up points in $\Delta\rho$ occur on the ascending portion of the pass, whereas the catch-up point in θ occurs on the descent.

The mechanism that causes the range separation catch-up effect is as follows. At the time of maneuver and shortly thereafter, the nominal and perturbed trajectories appear to be identical under short time spans. During this short period, the perturbed satellite has a greater velocity than the nominal satellite, and so progresses further in the same amount of time along the approximately shared trajectory. To the ground site, this apparent difference in position along the same trajectory is seen as the perturbed satellite being closer to the ground site than the nominal satellite ($\rho_{\text{perturbed}} < \rho_{\text{nominal}}$), resulting in a positive $\Delta\rho$. As the time scale increases and Kepler’s Third Law dominates over rectilinear motion, the relatively higher orbit of the perturbed satellite causes the approximately shared trajectory to diverge into two trajectories, with the nominal satellite being lower in altitude, closer to the ground site, and thus causing $\Delta\rho$ to decrease ($\dot{\rho}_{\text{perturbed}} < \dot{\rho}_{\text{nominal}}$). The location of the catch-up point ($\rho_{\text{nominal}} = \rho_{\text{perturbed}}$) along the pass is dependent on altitude (detailed in Section 4.3). Unlike angular separation θ , the range catch-up effect cannot be described by a region bounded in azimuth-elevation space.

The trends in range separation discussed above, and their differences from angular separation, are useful for maneuver detection in one respect. In regards to maneuver detection, the worst time to observe the satellite from an angles-only sensor is in the catch-up region, which encompasses a large portion of the descending pass. However, for a ranging sensor (i.e. radar), the best time to make an observation is as close to the set point as possible, where range separation ρ is maximized. The opposite can be said for the middle portion of the pass, where range separations are smaller (maneuver detection is harder) while angular separation is greater (maneuver detection is easier). This complementary dynamic between angles and range measurements is useful to a sensor tasking algorithm in that sensors of different types (angles-only vice angles-and-ranging) can be prioritized to observe the portions of the sky that each is best-suited.

Summarizing, given a positive-velocity maneuver, trajectories which progress nearly-directly overhead of a ground site experience a catch-up effect, where the lower trajectory catches up and overtakes the higher orbit. In the direct-overhead case, the two trajectories converge in angular separation for an instant during the descending pass. For near-overhead passes, an oval-shaped catch-up region can be defined in azimuth-elevation space by setting an upper bound on θ . The range separation catch-up effect occurs for all pass geometries, not just overhead passes, and is caused by the perturbed satellite appearing faster, yet on the same trajectory, as the nominal satellite for a short time in the ascending pass. The range catch-up effect cannot be described by a region bounded in azimuth-elevation space. Angles-only sensors are best-used to detect maneuvers (of the type studied here) when looking at the middle portions of passes; ranging sensors are best on the descending portion of a pass.

4.3 Altitude Sensitivity

Angular Separation All previous discussion has been restricted to $h = 400\text{km}$ orbits; this section examines trends in angular and range separation as orbit altitude is increased up to 1000km . Orbit altitudes of 600, 800, and 1000km where simulated; only show plots of the highest altitude are shown.

Figure 9 shows angular separation plotted against the South component of the sub-satellite point for $h = 1000\text{km}$ orbits. Angular separation θ is lesser with higher altitudes, caused by the high ratio of slant range to relative range, as can be seen in comparing Figures 6 and 9. Because of the larger SMA relative to the $h = 400\text{km}$ case, viewing

duration from the ground site is larger, corresponding to a larger horizon distance at the rise and set points. General trends with respect to shapes of the θ curves remain the same. The catch-up effect occurs at about the same relative region as in the lower altitude case (about mid-way through the descending pass). The longer passes associated with higher altitudes allow the ground site to view θ increase after decreasing for some values of ψ which, given a lower orbit, would have receded beyond the horizon by that time. Some of the trajectories that in the $h = 400km$ case were not visible long enough to experience the final increasing portion of the catch-up effect can be seen to increase in the $h = 1000km$ case; this is best seen in comparing the $\psi = 34^\circ$ trajectory in Figures 6 and 9. The $h = 600$ and $800km$ cases are consistent with the observations in the $h = 1000km$ case.

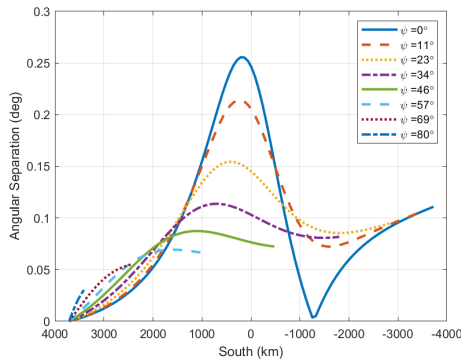


Fig. 9: Angular separation between the nominal and perturbed trajectories as observed from the ground site ($h = 1000km$, $\Delta V = 10m/s$).

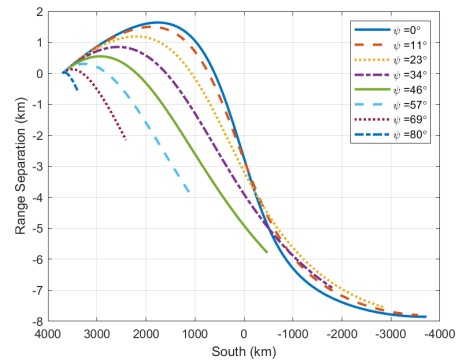


Fig. 10: Range separation between the nominal and perturbed trajectories as observed from the ground site ($h = 1000km$, $\Delta V = 10m/s$).

Figure 11 shows a catch-up region for $h = 1000km$ from $0^\circ < \beta < 21.8^\circ$ and $22.0^\circ < el < 44.6^\circ$. The catch-up effect occurs for a lesser range of initial headings at the higher altitude than for the lower altitude; at $h = 1000km$, the catch-up effect threshold is $\psi \lesssim 5.5^\circ$ (compared to 8.3° at $h = 400km$). Table 1 details the azimuth/elevation bounds for catch-up regions ($\theta < 0.05^\circ$) for all tested altitudes. The center of the region increases in elevation with altitude, equivalently stated as a catch-up event occurring earlier in a pass as altitude increases. This earlier occurrence of catch-up events is caused by the increased altitude allowing more time for the trajectories to diverge over a given portion of the pass compared to a lower orbit. This same effect also causes the range of catch-up region azimuth bounds (the width of the oval) to generally increase with increasing altitude. The azimuth size of the catch-up region slightly decreases in the altitude bin moving from 400 to $600km$; this counter to the trend is likely due to numerics when fitting a contour surface to the simulation data. The range of elevation bounds (the height of the oval) decreases with increasing altitude, driven by the large absolute distance to the satellites relative to the small relative distance between the satellites.

Table 1: Catch-up region bounds for $\theta < 0.05^\circ$ contours for different orbit altitudes. Note that symmetry about $\beta = 0$ doubles the size of the bounding box in that dimension ($\Delta V = 10m/s$).

Altitude (km)	β Bounds ($^\circ$)	el Bounds ($^\circ$)	Region Size ($\beta \times el$) ($^\circ$)	el Center ($^\circ$)
400	0 - 20.4	5.4 - 29.9	40.7×24.4	17.7
600	0 - 20.2	12.7 - 36.1	40.3×23.4	24.4
800	0 - 20.8	18.3 - 40.1	41.6×21.8	29.2
1000	0 - 21.8	22 - 44.6	43.6×22.6	33.3

Range Separation Figure 10 shows the range separation $\Delta\rho$ for the $h = 1000km$ case. The larger nominal SMA allows for a longer observation duration to view the trajectories diverging, which we see in larger (negative) magnitudes of $\Delta\rho$ ($-8km$ vice $-6km$ for the lower orbit). The shapes of the $\Delta\rho$ histories trend the same relative to their lower altitude counterparts as in the θ discussion; the trends are identical. Altitude does not meaningfully impact the evolution of range separation over space and time.

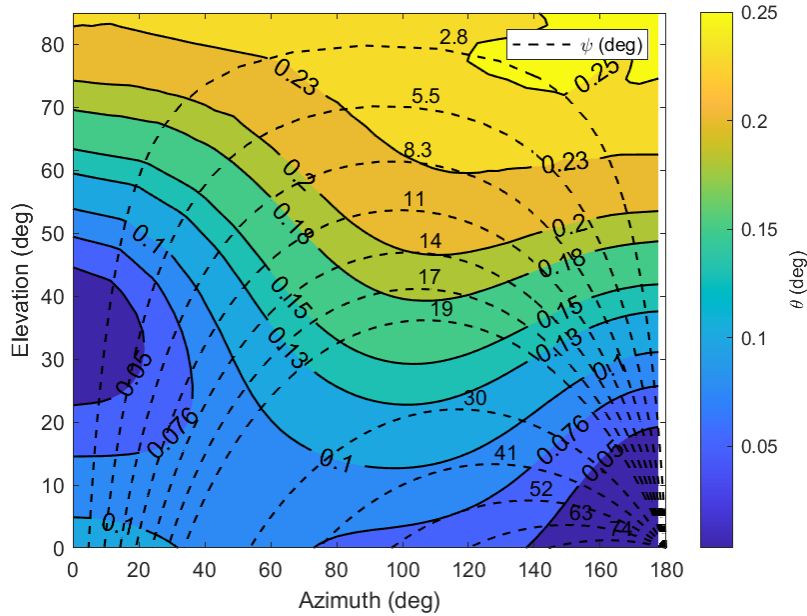


Fig. 11: Lines of initial heading ψ are overlaid on angular separation contours. All trajectories start at $\beta = 180^\circ, el = 0^\circ$. Elevation and azimuth correspond to nominal trajectories ($h = 1000\text{km}, \Delta V = 10\text{m/s}$).

Summarizing, altitude does not meaningfully impact the general trends of angular and range separation, although magnitude of the metrics is affected. The angular separation catch-up region occurs slightly earlier in the pass with increasing altitude (although stays in the descending portion of the pass for the altitudes tested). The catch-up region becomes smaller in elevation and larger in azimuth as altitude increases. Orbit altitude does not impact the conclusions regarding sensor tasking strategies discussed in Section 4.2.

4.4 Maneuver Magnitude Sensitivity

Previous analysis was performed with maneuver magnitudes of $\Delta V = 10\text{m/s}$. This section analyzes the sensitivity of θ catch-up regions with respect to ΔV . Table 2 shows catch-up region parameters for various ΔV magnitudes. The second row in Table 2 is identical to the first row in Table 1. Because order-of-magnitude changes in ΔV result in order-of-magnitude changes in angular separation θ , and the bound of a catch-up region is a design parameter, a different upper value for θ was selected for each maneuver magnitude (design and dependent variables are delimited by the double-vertical lines in Table 2). Because the bounds on θ are design variables, comparisons regarding catch-up region trends across θ (and ΔV) must be made cautiously. Given the linear relationship between the chosen ΔV and θ parameters, the catch-up bounding box size does not significantly change with deviations in ΔV . The location (elevation center) of the bounding box also does not change significantly with ΔV . Maneuver magnitude does not meaningfully impact the character of catch-up regions or sensor tasking strategy with regards to maneuver detection.

Table 2: Catch-up region bounds for different maneuver magnitudes ($h = 400\text{km}$).

$\Delta V(\text{m/s})$	θ Bound ($^\circ$)	β Bounds ($^\circ$)	el Bounds ($^\circ$)	Region Size ($\beta \times el$)($^\circ$)	el Center ($^\circ$)
1	0.005	0 - 20.3	5.5 - 29.8	40.5×24.3	17.7
10	0.05	0 - 20.4	5.4 - 29.9	40.7×24.4	17.7
100	0.5	0 - 21.2	4.8 - 30.3	42.4×25.5	17.5

5. CONCLUSION

In conclusion, the initial conditions chosen for this study (a single rise point and a half-fan of initial headings) are valid to observe trends over a single orbital pass because the assumptions built into said initial conditions do not break

down in the generalized cases. Due to the high ratio of slant range (site-to-satellite) to relative distance (satellite-to-satellite), angular separation increases and peaks as the nominal and perturbed trajectories approach the zenith point above the ground site. Given a positive-velocity maneuver, trajectories which progress nearly-directly overhead of a ground site experience a “catch-up” effect, where the lower trajectory catches up and overtakes the higher orbit. In the direct-overhead case, the two trajectories converge in angular separation for an instant during the descending pass. An oval-shaped catch-up region can be defined in azimuth-elevation space, centered on the convergence point, by setting an upper bound on angular separation. The range separation catch-up effect occurs on the ascending pass for all geometries, not just overhead passes, and is caused by the perturbed satellite appearing faster, yet on the same trajectory, as the nominal satellite for a short time after maneuver. The range separation catch-up cannot be described by azimuth-elevation region.

Changes in altitude do not majorly impact the trends of angular and range separation in time or space. Angular separation is lesser with higher altitudes, caused by the high ratio of slant range to relative range. The longer passes associated with higher altitudes allow the ground site to view angular separations increase, after decreasing, for some values of initial heading which, given a lower orbit, would have receded beyond the horizon by that time. Similarly, larger magnitudes of range separation are observed due to the extended viewing time of higher orbits. For angular separation, increased altitude corresponds with an earlier catch-up point. The greater slant range to relative range ratio for higher altitudes drives both narrower elevation and wider azimuth bounds of angular separation catch-up regions. Maneuver magnitude does not have a meaningful effect on catch-up region bounds or location.

The trends observed in angular and range separation, as well as the identification and characterization of the angular catch-up region can be used to inform maneuver or CSO detection algorithms in STM sensors. Angles-only sensors are best-used to detect maneuvers of the type studied here when looking at the middle portions of passes, where angular separation is large and before the catch-up region has been entered. Ranging sensors are best-used during the descending portion of a pass, where range separation is maximized.

REFERENCES

- [1] European Space Agency. (2022) ESA's annual space environment report. https://www.sdo.esoc.esa.int/environment_report/Space_Environment_Report_latest.pdf. Accessed: 2022-06-05.
- [2] D. Trump. (2018) Space policy directive-3, national space traffic management policy. <https://trumpwhitehouse.archives.gov/presidential-actions/space-policy-directive-3-national-space-traffic-management-policy/>. Accessed: 2022-06-01.
- [3] T. Harrison and K. Johnson. (2018) How does space policy directive 3 affect space traffic management. <https://www.csis.org/analysis/how-does-space-policy-directive-3-affect-space-traffic-management>. Center for Strategic and International Studies. Accessed: 2022-06-01.
- [4] J. Foust. (2021, July) Senators push for action on space traffic management. <https://spacenews.com/senators-push-for-action-on-space-traffic-management/>. Space News. Accessed: 2022-06-01.
- [5] S. Erwin. (2022) Office of space commerce to start developing architecture for traffic management. <https://spacenews.com/office-of-space-commerce-to-start-developing-architecture-for-traffic-management/>. Space News. Accessed: 2022-07-20.
- [6] 18th Space Control Squadron. (2020) Spaceflight safety handbook for satellite operators, version 1.5. https://www.space-track.org/documents/Spaceflight_Safety_Handbook_for_Operators.pdf. Accessed: 2022-06-01.
- [7] M. Holzinger and D. Scheeres, "Object correlation and maneuver detection using optimal control performance metrics," in *Advanced Maui Optical and Space Surveillance Technologies Conference (AMOS)*, 2010.
- [8] A. Pastor, G. Escribano, and D. Escobar, "Satellite maneuver detection with optical survey observations," in *Advanced Maui Optical and Space Surveillance Technologies Conference (AMOS)*, 2020.
- [9] D. A. Vallado, *Fundamentals of astrodynamics and applications*. Springer Science & Business Media, 2001, vol. 12.
- [10] J. G. Miller, "A new sensor allocation algorithm for the space surveillance network," *Military Operations Research*, pp. 57–70, 2007.
- [11] K. Hill, P. Sydney, K. Hamada, R. Cortez, K. Luu, M. Jah, P. Schumacher, M. Coulman, J. Houchard, and D. Naho'olewa, "Covariance-based network tasking of optical sensors," in *Paper AAS 10-150 presented at the AAS/AIAA Space Flight Mechanics Conference, February*, 2010, pp. 14–17.
- [12] T. A. Hobson and I. Clarkson, "Sensor-scheduling simulation of disparate sensors for space situational awareness," in *Proceedings of the Advanced Maui Optical and Space Surveillance Technologies Conference*, vol. 1. IEEE, 2011, p. 60.

A. ALGORITHM: ORBITAL PASS DESIGNER

Algorithm 1 Orbital Pass Designer (circular orbits)

Inputs : $\phi, \lambda, r_0, \beta_0, \psi$

Outputs : \vec{r}_0, \vec{v}_0

$$v_0 = \sqrt{\frac{\mu}{r_0}}$$

$$\vec{r}_{site,0} = \mathbf{site}(\phi, \lambda, h = 0)$$

▷ See [9]

$$\rho_0 = \sqrt{r_0^2 - r_{site,0}^2}$$

$$\vec{\rho}_0^{SEZ} = -Rot_3(\beta_0) \begin{bmatrix} \rho_0 \\ 0 \\ 0 \end{bmatrix}$$

$$\vec{r}_0 = \mathbf{razel2rv}(\rho_0, \beta_0, eI_0 = 0, \vec{r}_{site,0})$$

▷ See [9]

$$\vec{v}_0^{NTW} = Rot_1(\psi) \begin{bmatrix} 0 \\ v_0 \\ 0 \end{bmatrix}$$

$$\vec{v}_0 = \mathbf{ntw2rv}(\vec{r}_0, \vec{v}_0^{NTW})$$

▷ See [9]
